Biomaterials Science

ROYAL SOCIETY OF CHEMISTRY

PAPER

View Article Online
View Journal | View Issue

Cite this: *Biomater. Sci.*, 2026, **14**, 2649

Synergic cancer chemo-immunotherapy comprising combined doxorubicin and siRNA targeting CD47 co-delivered by a bola-amphiphilic dendrimer

Baoping Lian,†[a,b] Dandan Zhu,†[a] Peng Chen,[a,b] Zhihui Wang,[a] Fanzhen Meng,[a] Ran Yan,[c] Nikolay A. Pyataev[d] and Xiaoxuan Liu *[a]

Restoring antitumor immunity while enhancing the chemotherapy efficacy represents an optimistic strategy for cancer treatment. Enabling macrophage-mediated phagocytosis of cancer cells is pivotal for rehabilitating effective immune responses. However, its efficacy is often limited by elevated anti-phagocytic signals, such as CD47, and insufficient pro-phagocytic signals on cancer cells. We employed a synergic chemo-immunotherapeutic approach involving the chemotherapeutic agent doxorubicin (DOX) together with siRNA targeting CD47 (siCD47), co-delivered by a bola-amphiphilic dendrimer (bola4A) as a nanocarrier. The co-delivery system (bola4A/DOX/siCD47) was established by encapsulating DOX within the hydrophobic interior of dendrimer nanomicelles, while complexing the negatively charged siCD47 to the positively charged dendrimer surface. The bola4A/DOX/siCD47 effectively downregulated CD47 expression and attenuated the CD47-signal regulatory protein α (SIRPα) axis-mediated anti-phagocytic signal. Concurrently, DOX induced immunogenic cell death (ICD) and significantly increased the exposure of calreticulin (CALR), a pro-phagocytic signal that elicits immune response. Consequently, bola4A/DOX/siCD47 enhanced phagocytosis of tumor cells by macrophages and reprogrammed the tumor immunosuppressive microenvironment (TME) towards enhanced macrophage phagocytosis, dendritic cell maturation, T cell infiltration, and elevated secretion of pro-inflammatory cytokines. Altogether, bola4A/DOX/siCD47 exhibited a potent antitumor effect through the coordinated action of DOX with siCD47 and offers a promising approach for synergistic cancer chemo-immunotherapy.

Received 8th January 2026,
Accepted 1st April 2026

DOI: 10.1039/d6bm00031b

rsc.li/biomaterials-science

Immune cells, such as natural killer cells, macrophages and T cells, play a vital role in combating tumor progression.[1,2] Macrophages, the innate immune cells with scavenger function, play a pivotal role in cancer immunotherapy by engulfing cancer cells *via* phagocytosis and activating cytotoxic T cells by cross-presenting tumor antigens.[3] However, tumors develop intricate self-protection mechanisms to evade immune surveillance, thereby establishing an immunosuppressive tumor microenvironment (TME).[4,5] Within the TME, tumor-associated macrophages (TAMs) represent the predominant immune infiltrates, constituting approximately 50% of the immune cell population.[6] Tumor cells frequently upregulate anti-phagocytic signals on their surface to escape recognition and clearance by TAMs, thereby promoting immune evasion.[7,8] Consequently, the phagocytic capacity of macrophages is impaired, limiting their proficiency in mounting an effective immune response to eliminate the tumor cells.[8,9] Restoring this phagocytic function is crucial for reprogramming the immunosuppressive TME and offers a promising strategy for cancer immunotherapy.[10]

The phagocytic potency of macrophages on tumor cells critically relies not only on the blockade of the anti-phagocytic ("don't eat me") signals, but also on the recognition of the pro-phagocytic ("eat me") signals on the surface of cancer cells.[7,8] The transmembrane protein CD47 is an anti-phagocytic signal that is overexpressed on the surface of various tumor cells.[11] CD47 provides a "don't eat me" anti-phagocytic signal upon binding to macrophages *via* its receptor signal regulatory protein alpha (SIRPα), thereby attenuating the phagocytosis and letting tumor cells slip past immune surveillance and

[a]*State Key Laboratory of Natural Medicines, Joint International Research Laboratory of Target Discovery and New Drug Innovation (Ministry of Education), Jiangsu Key Laboratory of Drug Discovery for Metabolic Diseases, Center of Advanced Pharmaceuticals and Biomaterials, China Pharmaceutical University, Nanjing 211198, P. R. China. E-mail: xiaoxuanliu@cpu.edu.cn*
[b]*Aix-Marseille Université, 163 avenue de Luminy, 13288 Marseille, France*
[c]*Key Laboratory of Biomedical Functional Materials, China Pharmaceutical University, Nanjing 211198, P. R. China*
[d]*National Research Ogarev Mordovia State University, Bolshevistskaya Str. 68, 430005 Saransk, Russia*
†These authors contributed equally to this work.

clearance.[12] Blocking this CD47/SIRPα axis can inhibit the "don't eat me" signal and reactivate macrophage-based tumor cell engulfment.[12] In parallel, the restoration of an "eat me" pro-phagocytic signal can be achieved by displaying exposure of calreticulin (CALR) on the surface of tumor cells.[13,14] CALR, a multifunctional calcium-binding chaperone protein primarily found in the endoplasmic reticulum (ER) lumen, can interact with low-density lipoprotein receptor-related protein 1 (LRP1) on macrophages,[14] which remarkably promotes phagocytosis-based engulfment of tumor cells. Therefore, simultaneously inhibiting CD47 and upregulating CALR on the tumor cell surface is expected to enhance macrophage phagocytosis and consequently improve macrophage-based cancer immunotherapy.[15,16]

Biopharmaceutics, including antibodies and small interfering RNAs (siRNAs), are well-established tools for regulating protein expression or modulating protein function. For instance, anti-CD47 monoclonal antibodies have been employed to effectively block the anti-phagocytic signal mediated by the CD47/SIPRα axis.[9,17,18] However, their clinical application is often limited by adverse effects, such as induced anemia,[19,20] thrombocytopenia,[19] or neurotoxicity.[21] Alternatively, siRNA-based therapeutics[22,23] constitute an effective strategy to specifically downregulate CD47 expression selectively in tumor cells,[24,25] thereby suppressing the anti-phagocytic signal with potentially reduced systemic toxicity. Considering reports of certain anticancer therapeutics, such as doxorubicin (DOX), inducing the CALR exposure that is desirable for immunogenic cell death (ICD)[26,27] and pro-phagocytosis, we wished to test a dual therapeutic strategy promoting this pro-phagocytic signal while downregulating the anti-phagocytic signal with siRNA. Specifically, we wanted to apply siRNA targeting CD47 (siCD47) in concert with DOX to simultaneously inhibit CD47 expression and increase CALR exposure on the tumor cell surface and investigate the capacity of this combination to synergistically enhance the phagocytic potency of macrophages to achieve effective anti-tumor activity.

To allow any synergistic action of the combination therapy, we needed a system able to co-deliver siCD47 and DOX simultaneously to the same tumor cells. Among various drug delivery systems, dendrimers are becoming popular drug carriers due to their distinctive dendritic structure and cooperative multivalency characteristics.[28–30] Recently, amphiphilic dendrimers, which are hybrids of lipids and dendrimers with thoughtfully engineered hydrophobic segments and hydrophilic dendrons, have demonstrated exceptional performance in drug delivery by capitalizing on the delivery benefits provided by both polymer and lipid vectors, along with the distinctive structural properties of dendrimers.[31,32] Our previous studies have established a series of supramolecular drug delivery nanosystems based on the self-assembly of amphiphilic dendrimers, able to deliver a variety of pharmaceutical reagents, such as anticancer drugs,[33–36] nucleic acid therapeutics,[37–42] imaging agents *etc.*,[43–45] with excellent results, even outperforming the current first line treatment option. In particular, we have developed the bola-amphiphilic dendrimer, bola4A, consisting of a bi-polar hydrophobic chain featuring a reactive oxygen species (ROS)-sensitive thioacetal group at the center, along with two hydrophilic poly(amido amine) (PAMAM) dendrons attached at the chain terminals (Scheme 1A). By combining its structural dendritic properties with robust bola-lipid self-assembly characteristics, this dendrimer can effectively carry siRNA[46] and the anticancer drug imatinib.[47] Most importantly for selective delivery, the ROS-sensitive thioacetal group within the bola-amphiphilic dendrimer enables on-demand release of the loaded drugs precisely within cancer cells that have elevated ROS levels.

Motivated by the success of this ROS-responsive bola4A for delivering both anticancer drugs and siRNA, we sought to extend its application to the co-delivery of the ICD inducer DOX and the siRNA-targeting CD47 for synergic cancer chemo-immunotherapy. This chemo-immunotherapeutic approach aims to promote macrophage-based cancer immunotherapy while better harnessing the cytotoxic effect of chemotherapy. Specifically, the co-delivery strategy enables spatiotemporal modulation of anti-phagocytic and pro-phagocytic signals within the same cell, thereby maximizing the transmission of phagocytic signals to macrophages. Indeed, the co-delivery of DOX and siCD47 *via* bola4A effectively inhibited the anti-phagocytic signal (CD47) and upregulated the pro-phagocytic signal (CALR), restoring macrophage phagocytosis, reprogramming the tumor microenvironment and generating strong anti-tumor efficacy. This co-delivery system based on the bola-amphiphilic dendrimer thus represents a promising platform for combined cancer therapy.

Results and discussion

Successful establishment of the bola4A/DOX/siCD47 co-delivery nanosystem

Our previous study demonstrated that the bola-amphiphilic dendrimer bola4A possessed excellent biocompatibility and high drug-loading capacity, resulting in significantly enhanced anticancer effects.[47] Consistently, in this study, bola4A encapsulated DOX with near-quantitative efficiency, achieving a high drug-loading content of up to 44% (Fig. 1A). Notably, bola4A features a thioacetal group that is readily degraded upon ROS exposure, enabling selective drug release within cancer cells characterized by elevated ROS levels. We thus evaluated the anticancer activity of bola4A/DOX nanoparticles (NPs) in two ROS-rich cancer cell lines: murine melanoma B16F10 cells and murine triple-negative breast cancer (TNBC) 4T1 cells, as well as in their respective ROS-depleted counterparts (Fig. S1A and S1B). The bola4A/DOX NPs exhibited effective and dose-dependent antiproliferative effects, which were significantly attenuated following pretreatment with the ROS scavenger *N*-acetylcysteine (NAC) (Fig. 1B and C). Quantitative analysis revealed an 18-fold or 7-fold increase in IC_{50} values under ROS-suppressed conditions for B16F10 (0.12 μM *vs.* 2.19 μM) and 4T1 cells (0.43 μM *vs.* 2.80 μM), respectively. These findings confirm that bola4A/DOX NPs are capable of inducing

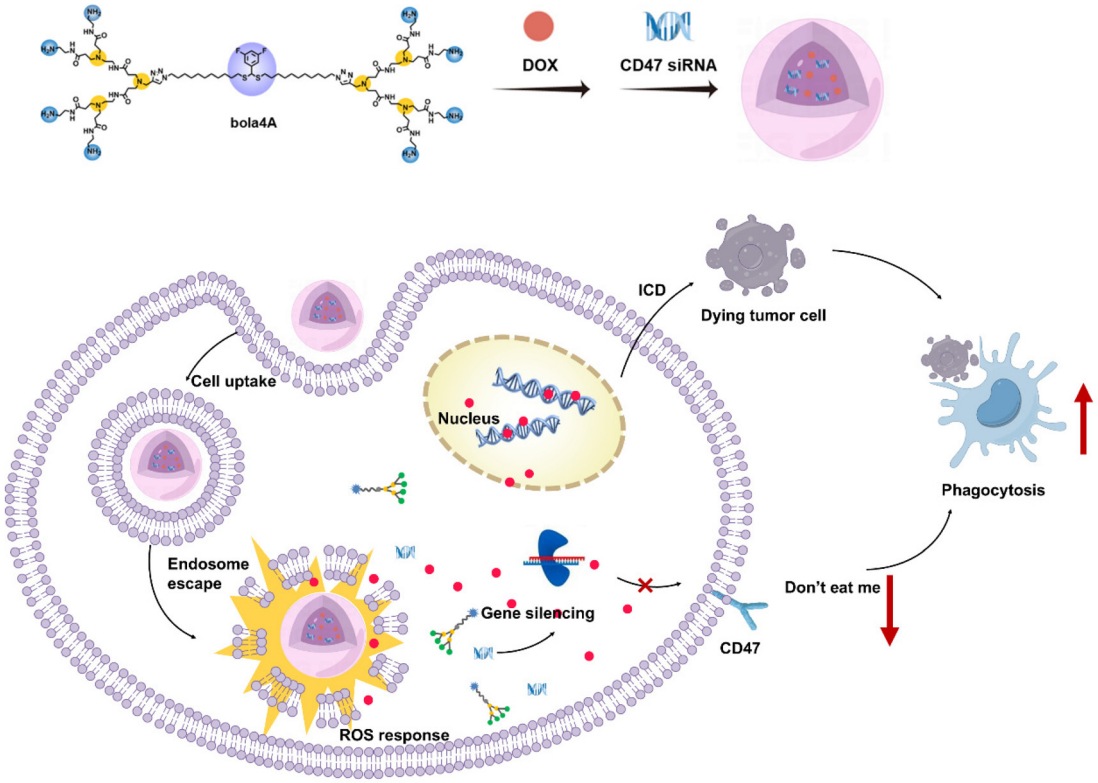

Scheme 1 Schematic illustration of bola4A in the co-delivery of DOX prodrug and siCD47 into tumor cells. Bola4A/DOX/siCD47 nanosystem mediated selective delivery of the anticancer drug DOX and siCD47 within cancer cells in response to high levels of ROS, which reawakened the phagocytic activity of macrophages *via* downregulation of CD47 expression and induction of ICD with chemotherapy for completely inhibiting tumor growth.

ROS-dependent drug release and, consequently, producing ROS-responsive anticancer activity.

Building on previous demonstrations of the bola4A-based nanosystem enabling ROS-responsive delivery of siRNA therapeutics,[37,46] we employed the DOX-loaded bola4A nanosystem to encapsulate siRNA targeting CD47 (siCD47). As shown in Fig. 1D and E, bola4A/DOX effectively retarded siRNA migration at an N/P $\geq$ 5, forming stable bola4A/DOX/siRNA complexes with an average hydrodynamic diameter of approximately 48.2 nm and a zeta potential of +17.2 mV as determined by dynamic light scattering (DLS). In comparison, bola4A/siRNA complexes measured 60.3 nm with a zeta potential of +21.1 mV, while bola4A/DOX particles were smaller (40.8 nm) and exhibited a higher zeta potential (+25.3 mV). Upon siRNA incorporation, the bola4A/DOX/siRNA complexes displayed intermediate particle size and surface charge values, consistent with partial surface neutralization by the negatively charged siRNA. Transmission electron microscopy (TEM) analysis (Fig. S2) further confirmed the formation of uniform spherical nanoparticles with an average diameter of approximately 40 nm. These results demonstrate that the DOX-loaded bola4A formulation retains a comparable capability for siRNA encapsulation to the bola4A dendrimer alone. In this co-delivery nanosystem, negatively charged siRNA binds electrostatically to the positively charged dendritic hydrophilic head groups of bola4A, while DOX is sequestered within the hydrophobic core *via* hydrophobic interactions. Moreover, this formulation effectively protects siRNA from enzymatic degradation (Fig. 1F).

To evaluate the ability of the bola4A/DOX/siRNA nanosystem to co-deliver siRNA and DOX into tumor cells, we assessed cellular uptake using Cy5-labelled siRNA by flow cytometry and confocal laser scanning microscopy (CLSM). As shown in Fig. S3A, both Cy5-siRNA and DOX fluorescence signals were detected in B16F10 and 4T1 cells following incubation with bola4A/DOX/Cy5-siRNA, with signal intensities increasing over time, indicating rapid and efficient internalization. Confocal images further confirmed strong intracellular green (Cy5) and red (DOX) fluorescence after 4 h (Fig. S3B), verifying efficient co-delivery of both cargos.

We next investigated the *in vivo* biodistribution of the bola4A/DOX/siCD47 nanosystem in orthotopic 4T1-luc tumor-bearing mice using the near-infrared fluorescent dye DiR and Cy5-labelled siRNA. *In vivo* fluorescence imaging revealed distinct and predominantly tumor-localized signals from both Cy5 and DiR within the bola4A/DOX/DiR/Cy5-siRNA nanosystem (Fig. S4). *Ex vivo* fluorescence imaging and quantitative analysis further confirmed significantly enhanced tumor

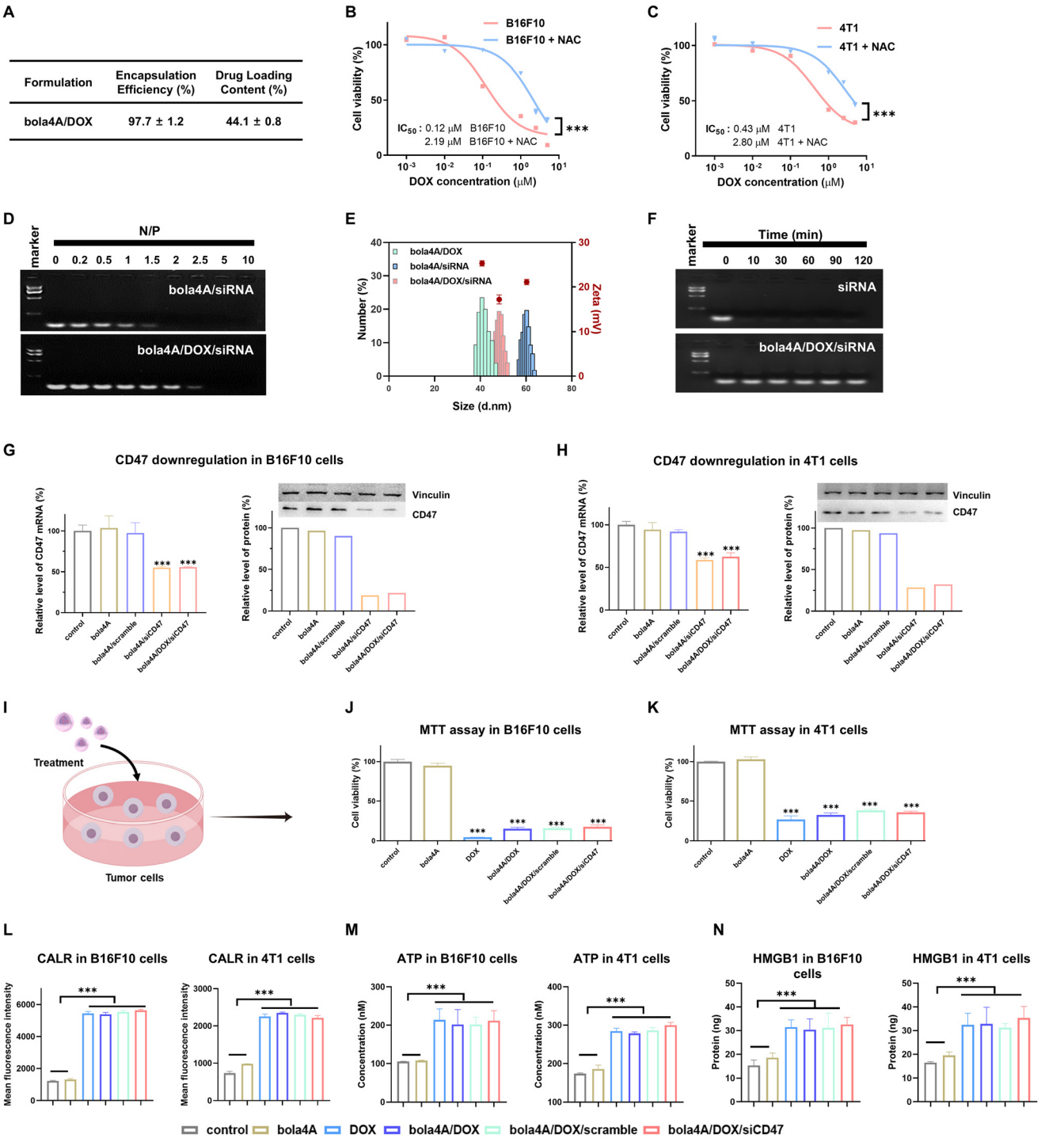

Fig. 1 Establishment of bola4A/DOX/siRNA co-delivery nanosystems and evaluation of their gene silencing efficacy and ICD induction. (A) Drug encapsulation efficiency of bola4A (mean ± SD, n = 3). (B and C) Antiproliferative effects of bola4A/DOX NPs on B16F10 (B) or 4T1 cells (C) in the absence and presence of *N*-acetylcysteine (NAC) (10 mM). (D) siRNA binding capacity of bola4A or bola4A/DOX NPs at varying N/P ratios (200 ng siRNA/well). (E) Size distribution and zeta potential of the bola4A/DOX/siRNA nanosystem measured by DLS analysis. (N/P ratio = 5, DOX: 3.6 μM, siRNA: 50 nM). (F) Protection of siRNA from enzymatic degradation, offered by bola4A/DOX (N/P ratio = 5, 200 ng siRNA/well). (G and H) CD47 mRNA expression (G) and CD47 protein (H) expression in B16F10 or 4T1 cells following treatment with the bola4A/DOX/siCD47 nanosystem (DOX: 3.6 μM, siRNA: 50 nM, N/P ratio = 5). (I) Schematic illustration of antiproliferative effects measured by MTT assays in B16F10 cells or 4T1 cells. (J and K) Cell viability assessed by the MTT assay in B16F10 (J) and 4T1 (K) cells treated with the bola4A/DOX/siCD47 nanosystem (DOX: 3.6 μM, siRNA: 50 nM, N/P ratio = 5). (L) Flow cytometric analysis of CALR surface exposure in treated B16F10 and 4T1 cells; the mean fluorescence intensity (MFI) of Alexa Fluor 647 is shown. (M and N) Quantification of extracellular ATP release (M) and HMGB1 secretion (N) from B16F10 or 4T1 cells after treatment with PBS, bola4A, DOX, bola4A/DOX, bola4A/DOX/scramble or bola4A/DOX/siRNA (DOX: 3.6 μM, siRNA: 50 nM, N/P ratio = 5) (one-way ANOVA followed by Tukey's multiple comparisons test was used to measure statistical significance. n = 3, ***p < 0.001).

accumulation of the bola4A/DOX/DiR/Cy5-siRNA nanosystem compared to PBS, free DiR, and free Cy5-siRNA controls. Importantly, relative to bola4A/Cy5-siRNA or bola4A/DOX/DiR formulations, the bola4A/DOX/DiR/Cy5-siRNA nanosystem achieved more efficient co-delivery of DOX and siRNA to the same tumor region (Fig. S5). Immunofluorescence staining corroborated these findings, demonstrating enhanced tumor enrichment of both therapeutic agents. Altogether, these results highlight the capability of the bola4A/DOX/siRNA nanosystem for simultaneous and effective delivery of chemotherapeutic agents and siRNA to tumors.

As described above, the ROS-responsive bola-amphiphilic dendrimer bola4A enables the simultaneous co-encapsulation of two distinct therapeutic modalities: the hydrophobic chemotherapeutic DOX and the hydrophilic nucleic acid therapeutic siRNA. This co-delivery approach offers a distinct advantage by integrating the direct cytotoxic effects of DOX with the gene-silencing activity of siRNA (*e.g.*, siCD47) within a single ROS-responsive nanocarrier.

CD47 silencing and ICD induction with retained DOX efficacy in the bola4A/DOX/siCD47 co-delivery nanosystem

Having established the stable bola4A/DOX/siCD47 nanosystem, we next investigated its capability to simultaneously suppress the anti-phagocytic signal CD47 and enhance the pro-phagocytic signal CALR. Both B16F10 and 4T1 cells treated with bola4A/siCD47 or bola4A/DOX/siCD47 showed ~50% downregulation of CD47 mRNA and ~80% reduction at the protein level relative to PBS and other controls (bola4A alone or bola4A/scramble) (Fig. 1G and H). The comparable silencing efficiency between bola4A/DOX/siCD47 and bola4A/siCD47 confirms effective siCD47 delivery by the co-loaded nanosystem without interference from DOX. Flow cytometry and confocal microscopy of B16F10 and 4T1 cells stained with anti-CD47-AF647 antibody revealed a marked decrease in surface CD47 expression after treatment with both nanosystems (Fig. S6A), consistent with efficient downregulation of this key anti-phagocytic marker. Importantly, while bola4A alone or bola4A/siCD47 showed negligible cytotoxicity, bola4A/DOX/siCD47 induced cytotoxicity comparable to free DOX or bola4A/DOX in both cell lines (Fig. 1I–K), demonstrating that siRNA incorporation does not compromise the chemotherapeutic efficacy of DOX.

We then assessed the activation of the pro-phagocytic signal induced by DOX-mediated ICD by the bola4A/DOX/siCD47 nanosystem. ICD is characterized by translocation of CALR to the plasma membrane, alongside extracellular release of danger-associated molecular patterns (DAMPs) such as ATP and high-mobility group box 1 (HMGB1), which promote dendritic cell (DC) maturation, macrophage polarization towards the pro-inflammatory M1 phenotype, and CD8+ T cell activation.[48–51] Treatment with free DOX, bola4A/DOX, or bola4A/DOX/siCD47 significantly increased CALR exposure on the plasma membrane of both B16F10 and 4T1 cells (Fig. 1L). Similarly, these treatments markedly enhanced ATP and HMGB1 release compared to PBS or bola4A alone (Fig. 1M and N). No significant differences in ICD markers were observed among the DOX-containing groups, confirming DOX as the primary ICD inducer and indicating that bola4A does not interfere with this process.

Finally, we evaluated the immunomodulatory effects of bola4A/DOX/siCD47 on bone marrow-derived dendritic cells (BMDCs) and macrophages (BMDMs) *in vitro*. Flow cytometry revealed upregulated expression of co-stimulatory molecules CD80, CD86, and the antigen-presenting molecule MHC-II on both BMDCs and BMDMs following treatment, indicating enhanced DC maturation and macrophage activation (Fig. S7). These findings demonstrate that bola4A/DOX/siCD47 effectively promotes immunogenic activation of antigen-presenting cells, consistent with ICD induction in tumor cells.

Synergistic enhancement of macrophage-mediated phagocytosis and antitumor effect *via* co-delivery of DOX and siCD47

Given that simultaneous downregulation of CD47 and increased CALR exposure on the tumor cell surface is expected to synergistically promote macrophage-mediated phagocytosis, we evaluated the pro-phagocytic potential of the bola4A/DOX/siCD47 nanosystem. B16F10 and 4T1 tumor cells were pretreated with different formulations, including PBS, bola4A, bola4A/siCD47, bola4A/DOX, and bola4A/DOX/siCD47, labeled with carboxyfluorescein succinimidyl ester (CFSE) and co-incubated with eFluor670-labeled BMDMs at a 4 : 1 tumor cell-to-macrophage ratio (Fig. 2A). Compared to the PBS and bola4A-alone controls, the single-agent treatments (bola4A/siCD47 and bola4A/DOX) moderately enhanced phagocytosis. Notably, the combination treatment (bola4A/DOX/siCD47) significantly augmented macrophage-mediated phagocytosis, with 3.0-fold and 4.6-fold enhancements in B16F10 and 4T1 cells, respectively, as quantified by flow cytometry (Fig. 2B). Confocal microscopy further confirmed enhanced co-localization of CFSE-labeled tumor cells (green) with eFluor670-labeled BMDMs (red), providing visual evidence of the occurrence of phagocytosis of tumor cells by BMDMs (Fig. 2C, white arrows).

We then assessed the synergistic antiproliferative effect resulting from combined chemotherapy and immunotherapy following enhanced phagocytosis. Luciferase-expressing tumor cells (B16F10-luc and 4T1-luc) were treated as above and co-cultured with BMDMs at the same ratio (Fig. 2D). Cell viability, quantified by D-Luciferin assay, revealed that bola4A/DOX/siCD47 treatment significantly inhibited tumor cell viability compared to single-agent groups.

Altogether, these findings demonstrate that the bola-amphiphilic dendrimer bola4A efficiently and selectively co-delivers siCD47 and DOX to tumor cells, effectuating CD47 downregulation (Fig. 1G and H) and increased CALR surface exposure (Fig. 1L). This dual modulation diminishes the anti-phagocytic signal while enhancing the pro-phagocytic cue, thereby promoting macrophage phagocytosis and potentiating antitumor immunity.

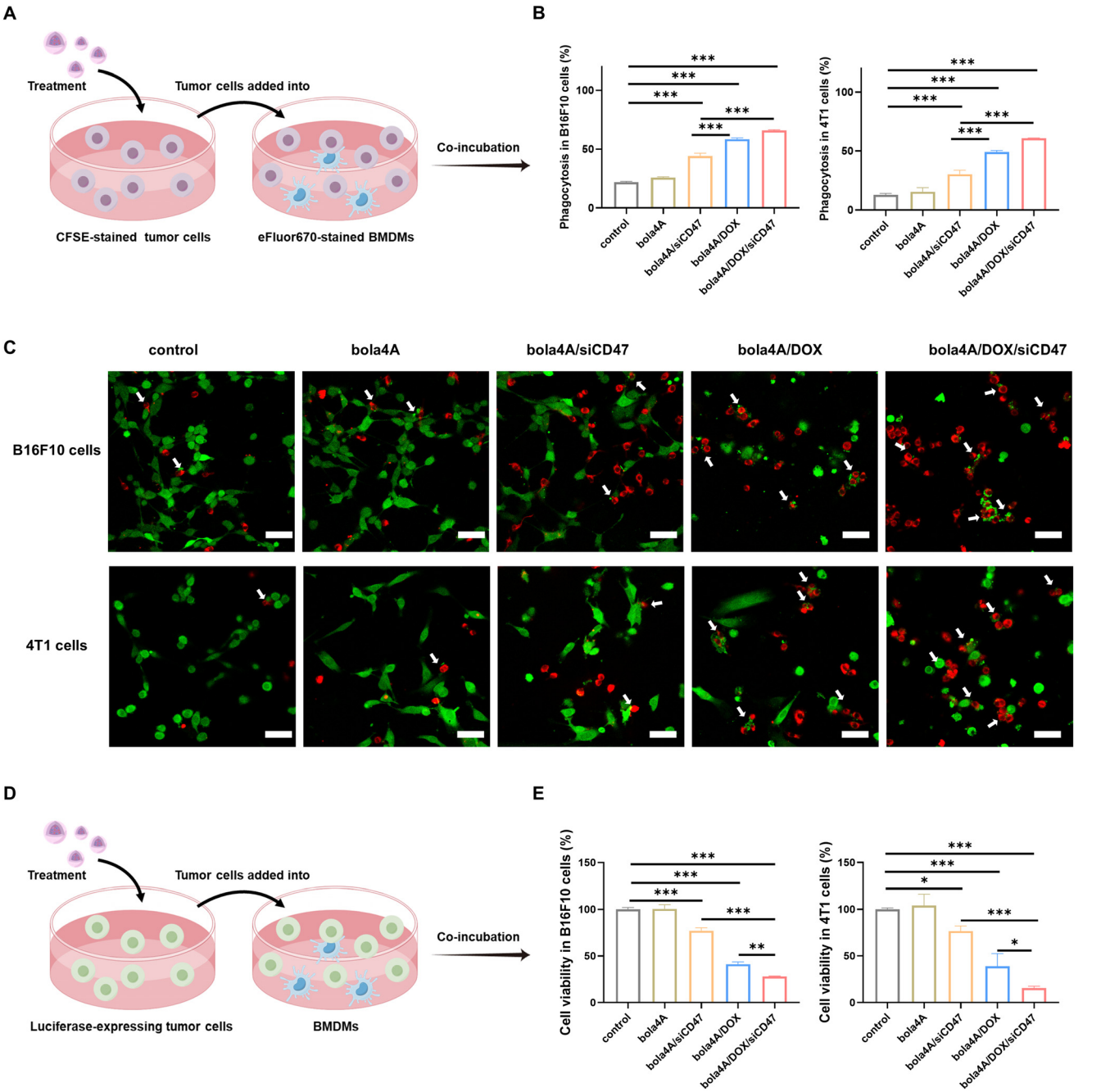

Fig. 2 Co-delivery nanosytem bola4A/DOX/siCD47 synergistically enhanced the phagocytosis of tumor cells by BMDMs. (A) Schematic illustration of the phagocytosis of tumor cells (B16F10 or 4T1) by BMDMs after various treatments, including PBS, bola4A, bola4A/siCD47 (siRNA: 50 nM, N/P ratio = 5), bola4A/DOX (DOX: 3.6 μM), and bola4A/DOX/siCD47 (DOX: 3.6 μM, siRNA: 50 nM, N/P ratio = 5). B16F10 or 4T1 cells labeled with CFSE and BMDM cells stained with eFlour®670. (B and C) Phagocytosis of B16F10 or 4T1 cells by BMDMs as determined by flow cytometry (B) and confocal microscopy (C) (scale bar = 50 μm). (D) Schematic illustration of the phagocytosis of firefly luciferase-expressing tumor cells (B16F10 or 4T1) by BMDMs after the various treatments. (E) Cell viability quantified by D-Luciferin assay (one-way ANOVA followed by Tukey's multiple comparisons test was used to measure statistical significance. $n = 3$, $^{*}p < 0.05$, $^{**}p < 0.01$; $^{***}p < 0.001$).

Potent anticancer efficacy and immune activation by bola4A/DOX/siCD47 in an orthotopic 4T1 TNBC model

Encouraged by the promising *in vitro* results, we evaluated the *in vivo* therapeutic efficacy of the bola4A/DOX/siCD47 nanosystem in an orthotopic 4T1 TNBC model, representative of an immunologically "cold" tumor type.[52,53] BALB/c mice bearing 4T1 tumors were randomized into six groups and treated *via* intravenous injection with PBS, free DOX, bola4A/DOX, bola4A/siCD47, bola4A/DOX/scramble, or bola4A/DOX/siCD47,

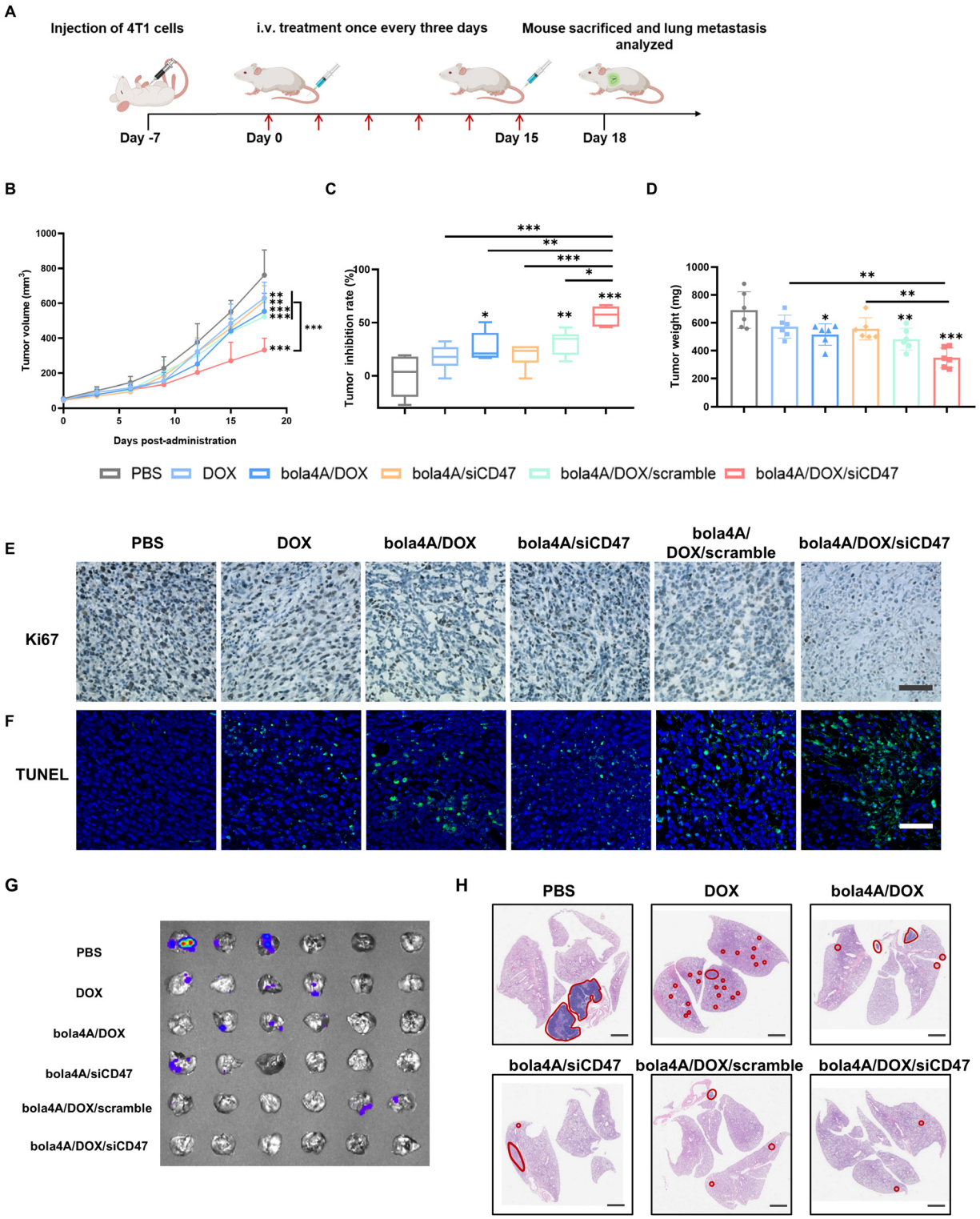

Fig. 3 *In vivo* anticancer activity of the bola4A/DOX/siCD47 nanosystem in the 4T1 orthotopic triple-negative breast cancer tumor mouse model. Mice were treated with PBS, free DOX (DOX: 2.5 mg kg^{-1}), bola4A/DOX (DOX: 2.5 mg kg^{-1}), bola4A/siCD47 (siRNA: 1 mg kg^{-1}), bola4A/DOX/scramble (DOX: 2.5 mg kg^{-1}, siRNA: 1 mg kg^{-1}, N/P ratio = 5), or bola4A/DOX/siCD47 (DOX: 2.5 mg kg^{-1}, siRNA: 1 mg kg^{-1}, N/P ratio = 5). (A) Treatment schedule for the 4T1 orthotopic tumor model. (B) Average tumor growth curves of 4T1-luc tumor-bearing mice following different treatments (n = 6). (C) Tumor growth inhibition rates. (D) Tumor weights measured after the final treatment. (E) Immunohistochemistry staining for Ki67 demonstrating tumor cell proliferation (scale bar, 50 μm). (F) TUNEL assay images showing apoptotic cells post-treatment (scale bar, 50 μm). (G) *Ex vivo* bioluminescence imaging of lung metastases at the experimental endpoint. (H) Histological analysis of lung tissues with metastatic lesions outlined in red (scale bar = 2 μm). Metastatic lesions were identified as cell clusters with densely stained nuclei. Data are presented as mean ± standard deviation (n = 6) (one-way ANOVA followed by Tukey's multiple comparisons test was used to measure statistical significance. n = 6, *p < 0.05, **p < 0.01, ***p < 0.001).

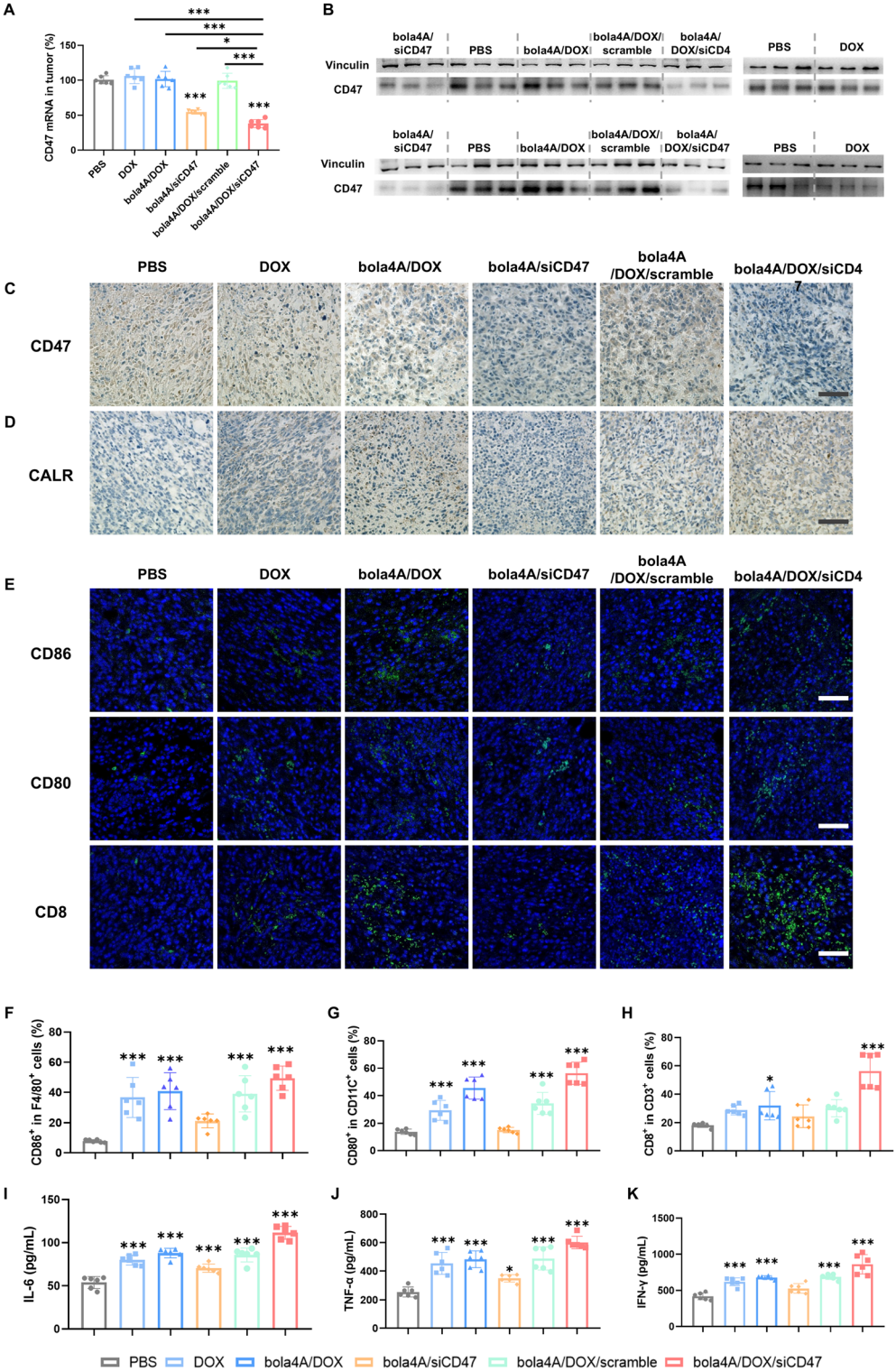

Fig. 4 *In vivo* immune activation by the bola4A/DOX/siCD47 nanosystem in the 4T1 orthotopic triple-negative breast cancer tumor mouse model. Mice were treated with PBS, free DOX (DOX: 2.5 mg kg^{-1}), bola4A/DOX (DOX: 2.5 mg kg^{-1}), bola4A/siCD47 (siRNA: 1 mg kg^{-1}), bola4A/DOX/scramble (DOX: 2.5 mg kg^{-1}, siRNA: 1 mg kg^{-1}, N/P ratio = 5), or bola4A/DOX/siCD47 (DOX: 2.5 mg kg^{-1}, siRNA: 1 mg kg^{-1}, N/P ratio = 5). (A) CD47 mRNA levels in tumor tissues measured by qRT-PCR. (B) CD47 protein expression in tumor tissues analyzed by western blotting. (C and D) Immunohistochemical staining of tumor tissues showing CD47 (C) and CALR (D) protein expression (scale bar = 50 μm). (E) Representative fluorescence immunohistochemistry and (F–H) flow cytometry cytometric quantification of immune cell populations within tumors, including M1 phenotype macrophages (CD86$^+$) (F), mature dendritic cells (CD80$^+$) (G), and CD8$^+$ T cells (H). (J–K) ELISA quantification of pro-inflammatory cytokines IL-6 (I), TNF-α (J) and IFN-γ (K) levels in tumor tissue following treatment. Data are presented as mean ± standard deviation (n = 6) (one-way ANOVA followed by Tukey's multiple comparisons test was used for statistical analysis, n = 6, *p < 0.05, **p < 0.01, ***p < 0.001).

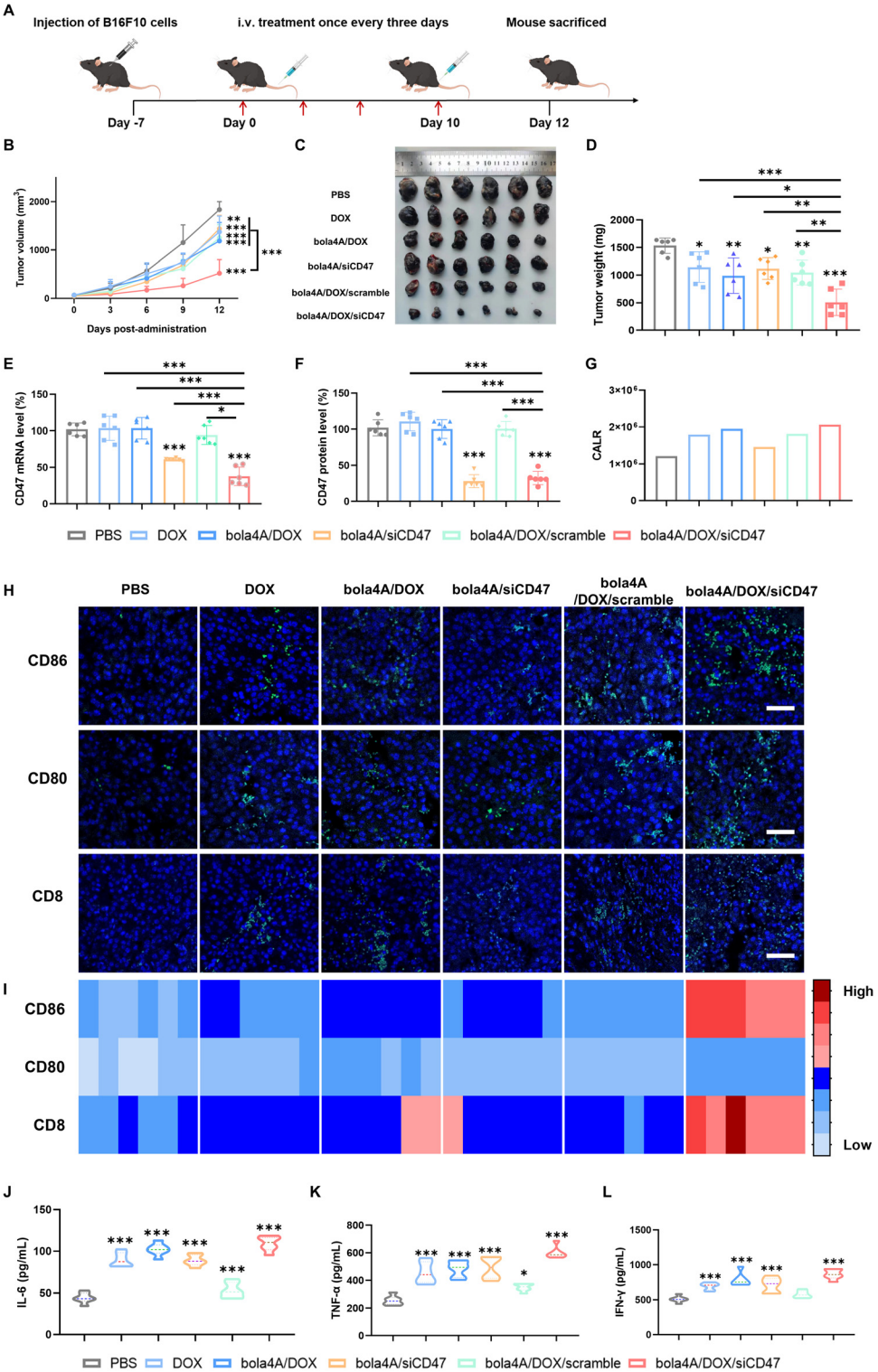

Fig. 5 *In vivo* anticancer activity and immune activation by the bola4A/DOX/siCD47 nanosystem in the B16F10 subcutaneous melanoma tumor mouse model. Mice were treated with PBS, free DOX (DOX: 2.5 mg kg^{-1}), bola4A/DOX (DOX: 2.5 mg kg^{-1}), bola4A/siCD47 (siRNA: 1 mg kg^{-1}), bola4A/DOX/scramble (DOX: 2.5 mg kg^{-1}, siRNA: 1 mg kg^{-1}, N/P ratio = 5), or bola4A/DOX/siCD47 (DOX: 2.5 mg kg^{-1}, siRNA: 1 mg kg^{-1}, N/P ratio = 5). (A) Treatment schedule. (B) Average tumor growth curves of treated mice (mean ± SD, n = 6). (C) Representative photographs and (D) weight of excised tumors at study endpoint. (E) qRT-PCR analysis of CD47 mRNA expression. (F) Western blot analysis of CD47 protein levels in tissues. (G) Quantification of CALR expression from IHC images using Image J. (H) Representative fluorescence IHC and (I) heat map of flow cytometry showing immune cells (n = 6). (J–L) ELISA analysis of pro-inflammatory cytokines IL-6 (J), TNF-α (K), and IFN-γ (L) levels in tumor tissue following treatments. One-way ANOVA followed by Tukey's multiple comparisons test was used to measure statistical significance (mean ± SD, n = 6, *p < 0.05, **p < 0.01, ***p < 0.001). Scale bar = 50 μm.

administered six times every three days (Fig. 3A). Single-agent treatments—DOX, bola4A/DOX, bola4A/siCD47, and bola4A/DOX/scramble—moderately inhibited tumor growth, achieving tumor growth inhibition (TGI) indices of 20–30% relative to PBS. In contrast, the combination bola4A/DOX/siCD47 treatment significantly enhanced the antitumor efficacy, achieving a 60% TGI (Fig. 3B and C). Endpoint tumor photographs (Fig. S8) and tumor weights (Fig. 3D) further confirmed the superior efficacy of the combination treatment. Immunohistochemical analysis of Ki67 and TUNEL staining revealed pronounced antiproliferative and pro-apoptotic effects following bola4A/DOX/siCD47 administration (Fig. 3E, F and Fig. S9A, B). Remarkably, histological examination of lungs showed fewer and smaller metastatic nodules after combination treatment, indicating potent metastasis inhibition (Fig. 3G and H). No significant changes were observed in the body weight (Fig. S10A), major organ histology (Fig. S10B), kidney/liver function, or hematological parameters (Fig. S10C), underscoring the favorable safety profile of the co-delivery system.

To elucidate the underlying mechanisms, we assessed the expression of CD47 in tumor tissues post-treatment. While CD47 mRNA and protein levels remained largely unchanged following DOX, bola4A/DOX, or bola4A/DOX/scramble treatments as compared to PBS, they were significantly downregulated in tumors treated with bola4A/siCD47 and bola4A/DOX/siCD47 (Fig. 4A–C and Fig. S11A), confirming effective siCD47 delivery. Concurrently, CALR exposure was markedly increased in tumors treated with DOX-containing formulations (bola4A/DOX and bola4A/DOX/siCD47), consistent with DOX-induced ICD (Fig. 4D and Fig. S11B).

Multiparameter immunofluorescence histochemistry revealed the highest infiltration of M1 phenotype macrophages ($CD86^+$), mature dendritic cells ($CD80^+$), and $CD8^+$ T cells within tumors following bola4A/DOX/siCD47 treatment compared to PBS and other groups (Fig. 4E). The percentage of M1 macrophages increased modestly with bola4A/DOX (40.8%), bola4A/siCD47 (21.1%), and bola4A/DOX/scramble (39.0%) relative to PBS (7.9%), but was most pronounced in the bola4A/DOX/siCD47 group (49.4%) (Fig. 4F). Similarly, DC maturation ($CD80^+$) and $CD8^+$ T cell infiltration were significantly elevated following combination therapy (Fig. 4G and H). Correspondingly, ELISA quantification of tumor cytokines revealed markedly increased secretion of interleukin-6 (IL-6), interferon-gamma (IFN-γ), and tumor necrosis factor-alpha (TNF-α) in bola4A/DOX/siCD47-treated tumors (Fig. 4I–K).

Collectively, these results demonstrate that bola4A/DOX/siCD47 treatment effectively downregulates CD47 expression and upregulates CALR on tumor cells, thereby enhancing macrophage-mediated phagocytosis and eliciting robust macrophage- and T cell-mediated antitumor immune responses. This dual modulation promotes infiltration of antitumo immune cells and cytokine production, culminating in potent macrophage-based immunotherapy in the 4T1 TNBC model.

Bola4A/DOX/siCD47 activates anticancer immune responses in a B16F10 melanoma model

Promoted by the enhanced phagocytosis of B16F10 cells by BMDMs observed following bola4A/DOX/siCD47 treatment, we assessed the antitumor efficacy of this nanosystem in a B16F10 melanoma model, characterized by high invasiveness, therapeutic resistance, and poor prognosis.[54] Treatment commenced when tumors reached approximately 50 mm^3, with intravenous injections of PBS, free DOX, bola4A/DOX, bola4A/siCD47, bola4A/DOX/scramble, or bola4A/DOX/siCD47 administered four times every three days (Fig. 5A). By day 12 post-treatment, bola4A/DOX/siCD47 elicited the most pronounced tumor growth inhibition (~70%) alongside significant suppression of tumor cell proliferation and increased apoptosis compared to all other groups (Fig. 5B and Fig. S12). Tumor volume and weight measurements corroborated this enhanced efficacy (Fig. 5C and D). No significant changes were observed in body weight (Fig. S13A), major organ histopathology (Fig. S13B), or blood biochemistry (Fig. S13C), indicating minimal systemic toxicity.

Mechanistically, bola4A/DOX/siCD47 efficiently silenced CD47 expression at both mRNA and protein levels (Fig. 5E, 5F and Fig. S14A, B) and induced CALR exposure (Fig. 5G and Fig. S14C). Immunophenotyping of the TME revealed a significant increase in M1 macrophages ($CD86^+$), mature dendritic cells ($CD80^+$), and $CD8^+$ T cells following bola4A/DOX/siCD47 treatment compared to PBS and other controls (Fig. 5H, I and Fig. S15), indicative of a robust and durable antitumor immune response. Correspondingly, plasma levels of proinflammatory cytokines IL-6, IFN-γ and TNF-α were markedly elevated (Fig. 5J–L), reflecting systemic immune activation.

Altogether, these results demonstrate that bola4A/DOX/siCD47, by concurrently suppressing the anti-phagocytic signal CD47 and enhancing the pro-phagocytic signal CALR, effectively reprograms the TME. This is evidenced by increased infiltration of macrophages and $CD8^+$ T cells, promotion of DC maturation, and elevated secretion of immunostimulatory cytokines, culminating in superior therapeutic efficacy in the B16F10 melanoma model.

Conclusion

In summary, we have developed a synergic chemo-immunotherapeutic approach that enhances macrophage-mediated phagocytosis to potentiate the antitumor effects of chemotherapy and innate immunity. This was accomplished by co-delivering the chemotherapeutic agent DOX and siRNA targeting the anti-phagocytic signal CD47 (siCD47) using the bola-amphiphilic dendrimer bola4A as a carrier. The bola4A/DOX/siCD47 nanosystem induced CALR exposure on tumor cell surfaces, thereby amplifying the pro-phagocytic "eat me" signal, while simultaneously silencing CD47 to attenuate the SIRPα-mediated anti-phagocytic "don't eat me" signal. This dual modulation significantly enhanced macrophage phagocytosis of tumor cells. By integrating immunotherapy-induced phagocytic activity with the cytotoxicity of DOX, bola4A/DOX/

siCD47 displayed significantly improved antitumor efficacy in both orthotopic 4T1 breast cancer and B16F10 melanoma models. The potent anticancer immune response was accompanied by TME remodeling, characterized by increased macrophage phagocytosis, DC maturation, $CD8^+$ T cell infiltration, and elevated pro-inflammatory cytokine secretion. This synergistic approach, combining chemotherapy with immune modulation, offers a promising avenue for the development of more effective cancer therapies.

Methods

Preparation of a drug-loaded bola4A nanosystem

The bola4A was used to encapsulate doxorubicin (DOX) *via* the film dispersion method according to the literature.[36,47] Briefly, DOX hydrochloride (ranging from 1.6 to 3.0 mg) was dissolved in 1.0 ml mixed solvent (chloroform/methanol = 3/2, vol/vol). Then, triethylamine (molar ratio of DOX/triethylamine = 1/3) was added to obtain hydrophobic DOX. The drug was mixed with 3.0 mg of bola4A in 3.0 ml of mixed solvent at 15 : 12 (bola4A : DOX) mass ratio with constant stirring. The solvent was removed by vacuum rotary evaporation to form a dry film. The dried film was then hydrated with distilled water at 50 °C for 30 minutes under sonication. The unloaded DOX was removed by filtration through a 0.22 μm polycarbonate membrane (Pall, Port Washington, NY, USA). The amount of DOX encapsulated in the micelles was measured using a multimode microplate reader (Cytation5, BioTek, Vermont, US) with the excitation wavelength at 477 nm and the emission wavelength at 591 nm.

Empty bola4A nanoformulation was prepared using the same procedures without DOX addition.

The drug-loading content and drug encapsulation efficiency were calculated as below:

$$\text{Drug loading content } (\%) = W_t/W_s \times 100\%$$

$$\text{Encapsulation efficiency } (\%) = W_t/W_o \times 100\%$$

W_t represents the amount of DOX that loaded into nanoparticles; W_o represents the initial amount of DOX fed; W_s represents the amount of nanoparticles after lyophilization.

Preparation of a drug and siRNA-loaded bola4A nanosystem

The bola4A dendrimer or bola4A/DOX was diluted to the desired concentration, and siRNA was dissolved in nuclease-free water at a predetermined concentration. The two solutions were mixed at various N/P ratios—where N/P represents the molar ratio of positively charged amine groups (N) on the dendrimer to negatively charged phosphate groups (P) on the siRNA backbone—and incubated at room temperature for 30 minutes to enable electrostatic complexation and formation of the complexes.

Gel retardation analysis of bola4A/DOX/siRNA complexes

The bola4A or bola4A/DOX was diluted to a suitable concentration, and siRNA was dissolved in nuclease-free water. The two solutions were then mixed at varying N/P ratios ranging from 0.2 to 10 and incubated for 30 minutes. Each sample contained a final nucleic acid concentration of 200 ng per well. The resulting complexes (bola4A/siRNA or bola4A/DOX/siRNA) were analyzed by electrophoretic mobility shift assay using 1% agarose gel in 1× TAE buffer at a constant voltage for 15 minutes. Nucleic acid bands were stained with GoodView nucleic acid dye and visualized using a Tanon 5200Multi automatic chemiluminescence imaging system (Tanon, Shanghai, China).

Dynamic light scattering (DLS)

The hydrodynamic diameter, polydispersity index (PDI), and zeta potential of the bola4A/DOX, bola4A/siRNA, and bola4A/DOX/siRNA complexes were measured using dynamic light scattering (DLS) on a NanoBrook Omni instrument (Brookhaven Instruments, USA).

RNase stability assessment of bola4A/DOX/siRNA complexes

The bola4A/DOX/siRNA complexes were prepared at an N/P ratio = 5, with a final nucleic acid concentration of 200 ng per sample. These samples were incubated with RNase A (1.0 μg ml^{-1}) at 37 °C for different time periods (0, 10, 30, 60, 90, and 120 minutes). After incubation, each sample was mixed with 0.50 μL of 1% SDS solution on ice to terminate the reaction. The integrity of the complexes was then analyzed by electrophoretic mobility shift assay (EMSA) on a 1% agarose gel in 1× TAE buffer, run at a constant voltage for 15 minutes. Nucleic acid bands were visualized by staining with GoodView nucleic acid dye and imaging with a Tanon 5200Multi automatic chemiluminescence system (Tanon, Shanghai, China).

In vitro siRNA transfection

4T1 or B16F10 cells were seeded in 6-well plates at a density of 8×10^4 cells per well in complete medium supplemented with 10% FBS. Prior to transfection, bola4A/siCD47 or bola4A/DOX/siCD47 complexes were prepared at an N/P ratio = 5 in serum-free medium. The cells were then incubated with the complexes for 8 hours. After replacing the transfection mixture with fresh complete medium, the cells were cultured for an additional 48 hours under standard conditions. The silencing efficiency of the target gene was evaluated by RT-qPCR and western blot analysis.

In vitro assessment of immunologic cell death (ICD)

4T1, B16F10 cells were seeded in 24-well plates at 5×10^4 cells per well for attachment and treated with or without bola4A/DOX for 24 hours. Cells were collected and incubated with anti-CD16/32 antibody for 30 minutes at 4 °C. Then, cells were further stained with anti-calreticulin antibody for 1 h at 37 °C and Alexa Fluor 488 secondary antibody for 30 minutes at 37 °C. After that, cells were washed three times with PBS and analyzed by flow cytometry. In addition, to detect the HMGB1 and ATP secretion from cancer cells, the supernatant was collected and measured using the HMGB1 ELISA kit and ATP determination kit (Beyotime, China).

In vitro assessment of phagocytosis

For flow cytometry, BMDMs isolated from C57BL/6 mice were stained with eFluor™ 670 (eBioscience, USA) and seeded into 24-well plates at a density of 1.25×10^4 cells per well to allow adhesion. Prior to co-culture, the medium was replaced with serum-free DMEM for 2 hours. Tumor cells were pretreated with various drugs for 24 hours to ICD and then labeled with the live-cell proliferation dye CFSE (Beyotime, China). These labeled tumor cells were co-cultured with the eFluor 670-labeled BMDMs at a 4 : 1 ratio (5×10^4 total cells per well) for 12 hours. After co-culture, all cells were collected, washed three times with PBS, and resuspended in PBS for flow cytometric analysis. The phagocytosis rate was calculated as the percentage of double-positive BMDMs ($CFSE^+$ eFluor 670^+) among the total eFluor 670^+ BMDM population.

For confocal microscopy analysis, the same method described above was used, except that cells were seeded into confocal imaging dishes. After co-culture, cells were fixed and processed for imaging by confocal microscopy.

In vitro anticancer activity assay

Firefly Luciferase Assay: 4T1-luc or B16F10-luc cells were seeded in 24-well plates at 5×10^4 cells per well. Tumor cells were first treated with different formulations for 24 hours. Then, they were co-cultured with or without BMDMs for 12 hours at a 4 : 1 ratio. After co-culture, all cells were collected and incubated with 0.15 mg ml^{-1} fluorescein sodium salt solution. Bioluminescent signals were measured using a multimode microplate reader.

In vivo anticancer effect

All animal experiments were approved by the Animal Ethics Committee of China Pharmaceutical University (approval numbers are 2023-12-026 and 2023-12-027) and conducted in accordance with the national guidelines for animal protection.

When the average tumor volume reached approximately 50 mm^3 in the subcutaneous B16F10 melanoma or orthotopic 4T1 breast cancer model, mice were randomly assigned to six groups (n = 6 per group) and administered intraperitoneal injections every three days, totaling four doses for the melanoma model and six doses for the breast cancer model, respectively. The treatment groups were as follows: PBS, DOX (DOX: 2.5 mg kg^{-1}), bola4A/DOX (DOX: 2.5 mg kg^{-1}), bola4A/siCD47 (siRNA: 1 mg kg^{-1}), bola4A/DOX/scramble (DOX: 2.5 mg kg^{-1}, siRNA: 1 mg kg^{-1}, N/P ratio = 5), and bola4A/DOX/siCD47 (DOX: 2.5 mg kg^{-1}, siRNA: 1 mg kg^{-1}, N/P ratio = 5). Tumor volumes were measured using a caliper and calculated according to the formula: volume = length × $width^2$ × 0.5.

In vivo antitumor mechanism

Following the final treatment, the mice were euthanized and tumor tissues were collected. The tumors were mechanically homogenized, and the resulting suspensions were subjected to western blot analysis for CD47 protein expression and RT-qPCR for CD47 mRNA quantification.

Additionally, tumor samples were washed with PBS, fixed in 4% paraformaldehyde (PFA), dehydrated overnight, and embedded in paraffin. Tissue sections were then incubated with antibodies against Ki67,[55] CD47, and CALR and subjected to TUNEL staining according to standard protocols. All stained sections were imaged and analyzed using laser scanning confocal microscopy.

In vivo antitumor immune response

To investigate the infiltration of different immune cells in the tumor microenvironment, all mice were euthanized three days after the final treatment. The harvested tumors were gently minced into small fragments and digested in cell culture media supplemented with 1.0 mg ml^{-1} type IV collagenase and 0.1 mg ml^{-1} DNase I at 37 °C for 30 minutes. The resulting suspension was filtered through a 70 μm strainer to obtain single cells. Red blood cells (RBCs) were removed, and the remaining cells were blocked with anti-CD16/32 (BD Biosciences, USA) for 20 minutes at 4 °C. Subsequently, the cells were stained with the following fluorescence-labeled antibodies. After three washes with PBS, the stained cells were analyzed by flow cytometry.

The remaining tumor tissues were washed with PBS, fixed in 4% paraformaldehyde (PFA), dehydrated overnight, and embedded in paraffin. Tissue sections were incubated with Alexa Fluor 488-conjugated anti-CD8 (AiFang, China), anti-CD86 (AiFang, China), and anti-CD80 (Thermo Scientific, USA) antibodies. Following DAPI counterstaining, all sections were examined using laser confocal microscopy.

For cytokine analysis, mice were euthanized post-treatment, and tumor tissues were collected and homogenized in cold PBS to generate single-cell suspensions. The homogenates were centrifuged, and supernatants were used for cytokine detection. Intratumoral levels of IFN-γ, IL-1β, and TNF-α were quantified using ELISA kits.

Statistical tests

All data are presented as mean ± SD unless otherwise indicated. Statistical analysis was performed by one-way analysis of variance (ANOVA), two-way ANOVA, unpaired Student's t-test or the Mann–Whitney test (GraphPad Prism 8.01). A p value <0.05 was considered statistically significant, whereby all significant values in various figures are indicated as follows: $*p \leq 0.05$; $**p \leq 0.01$; $***p \leq 0.001$

Author contributions

BL: methodology, investigation, data curation, and writing – original draft preparation. DZ: investigation, data curation, and writing – reviewing and editing. PC: synthesis, investigation, and data curation. ZW & FM: investigation and formal analysis. RY: formal analysis. NA Pyataev: writing – reviewing and editing. XL: conceptualization, methodology, project administration, and writing – reviewing and editing.

Conflicts of interest

The authors declare that they have no known competing financial interests or personal relationships that could have appeared to influence the work reported in this paper.

Ethical statement

All animal procedures were performed in accordance with the Guidelines for Care and Use of Laboratory Animals of China Pharmaceutical University and approved by the Animal Ethics Committee of China Pharmaceutical University.

Data availability

The data supporting this article have been included as part of the supplementary information (SI). Supplementary information: materials and detailed experimental procedures. See DOI: https://doi.org/10.1039/d6bm00031b.

Acknowledgements

This work was financially supported by the National Natural Science Foundation of China (No. 82572431, 51773227), the National Technology Innovation Center for Biopharmaceuticals (No. NCTIB2023XB02003), the National Key Research & Development Program of China for International S&T Cooperation Projects (No. 2018YFE0117800), the Youth Thousand-Talents Program of China, the CAI YUAN PEI program (P. C.) and the China Scholarship Council (B. L.). We thank Dr Ling Peng (Aix-Marseille University – CNRS) for her assistance in reviewing and editing the manuscript. We also thank Ms. Jie Zhao (Animal Experimental Center, China Pharmaceutical University) for her assistance in animal experiments and Ms. Xiaozhen Yang (Public Experimental Platform, China Pharmaceutical University) for her assistance in the transmission electron microscopy characterization.

References

1 R. Medzhitov and A. Iwasaki, *Cell*, 2024, **187**, 2079–2094.
2 A. Hu, L. Sun, H. Lin, Y. Liao, H. Yang and Y. Mao, *Signal Transduct. Target. Ther.*, 2024, **9**, 68.
3 D. M. Mosser, K. Hamidzadeh and R. Goncalves, *Cell. Mol. Immunol.*, 2021, **18**, 579–587.
4 A. Marçais and T. Walzer, *Nat. Med.*, 2018, **24**, 260–261.
5 M. Mohme, S. Riethdorf and K. Pantel, *Nat. Rev. Clin Oncol.*, 2017, **14**, 155–167.
6 L. Cassetta and J. W. Pollard, *Nat. Rev. Drug Discovery*, 2018, **17**, 887–904.
7 Y. e. Liu, Y. Wang, Y. Yang, L. Weng, Q. Wu, J. Zhang, P. Zhao, L. Fang, Y. Shi and P. Wang, *Signal Transduct. Target. Ther.*, 2023, **8**, 104.
8 M. Feng, W. Jiang, B. Y. S. Kim, C. C. Zhang, Y.-X. Fu and I. L. Weissman, *Nat. Rev. Cancer*, 2019, **19**, 568–586.
9 S. Chen, S. W. T. Lai, C. E. Brown and M. Feng, *Front. Immunol.*, 2021, **12**, 635173.
10 A. Mantovani, P. Allavena, F. Marchesi and C. Garlanda, *Nat. Rev. Drug Discovery*, 2022, **21**, 799–820.
11 S. B. Willingham, J.-P. Volkmer, A. J. Gentles, D. Sahoo, P. Dalerba, S. S. Mitra, J. Wang, H. Contreras-Trujillo, R. Martin, J. D. Cohen, P. Lovelace, F. A. Scheeren, M. P. Chao, K. Weiskopf, C. Tang, A. K. Volkmer, T. J. Naik, T. A. Storm, A. R. Mosley, B. Edris, S. M. Schmid, C. K. Sun, M.-S. Chua, O. Murillo, P. Rajendran, A. C. Cha, R. K. Chin, D. Kim, M. Adorno, T. Raveh, D. Tseng, S. Jaiswal, P.Ø Enger, G. K. Steinberg, G. Li, S. K. So, R. Majeti, G. R. Harsh, M. v. d. Rijn, N. N. H. Teng, J. B. Sunwoo, A. A. Alizadeh, M. F. Clarke and I. L. Weissman, *Proc. Natl. Acad. Sci. U. S. A.*, 2012, **109**, 6662–6667.
12 Y. Hao, X. Zhou, Y. Li, B. Li and L. Cheng, *Int. Immunopharmacol.*, 2023, **120**, 110255.
13 M. P. Chao, S. Jaiswal, R. Weissman-Tsukamoto, A. A. Alizadeh, A. J. Gentles, J. Volkmer, K. Weiskopf, S. B. Willingham, T. Raveh, C. Y. Park, R. Majeti and I. L. Weissman, *Sci. Transl. Med.*, 2010, **2**, 63ra94.
14 S. J. Gardai, K. A. McPhillips, S. C. Frasch, W. J. Janssen, A. Starefeldt, J. E. Murphy-Ullrich, D. L. Bratton, P.-A. Oldenborg, M. Michalak and P. M. Henson, *Cell*, 2005, **123**, 321–334.
15 H. Huang, Q.-S. Tong, J.-Y. Zhang, W.-M. Miao, H.-H. Yu, J. Wang, S. Shen and J.-Z. Du, *Adv. Mater.*, 2025, **37**, e2500982.
16 J.-Q. Luo, R. Liu, F.-M. Chen, J.-Y. Zhang, S.-J. Zheng, D. Shao and J.-Z. Du, *ACS Nano*, 2023, **17**, 8966–8979.
17 Z. Jiang, H. Sun, J. Yu, W. Tian and Y. Song, *J. Hematol. Oncol.*, 2021, **14**, 180.
18 Z.-H. Ye, W.-B. Yu, M.-Y. Huang, J. Chen and J.-J. Lu, *Acta Pharm. Sin. B*, 2023, **13**, 1467–1487.
19 L. Johnson, R. K. Pillai, R. L. King, S. M. Ansell, R. W. Chen, I. Flinn, M. B. Maris, M. Irwin, E. L. Sievers, P. S. Petrova and R. A. Uger, *J Clin Oncol.*, 2017, **35**, 112.
20 R. W. Velliquette, J. Aeschlimann, J. Kirkegaard, G. Shakarian, C. Lomas-Francis and C. M. Westhoff, *Transfusion*, 2019, **59**, 730–737.
21 S. Gholamin, S. S. Mitra, A. H. Feroze, J. Liu, S. A. Kahn, M. Zhang, R. Esparza, C. Richard, V. Ramaswamy, M. Remke, A. K. Volkmer, S. Willingham, A. Ponnuswami, A. McCarty, P. Lovelace, T. A. Storm, S. Schubert, G. Hutter, C. Narayanan, P. Chu, E. H. Raabe, G. H. IV, M. D. Taylor, M. Monje, Y.-J. Cho, R. Majeti, J. P. Volkmer, P. G. Fisher, G. Grant, G. K. Steinberg, H. Vogel, M. Edwards, I. L. Weissman and S. H. Cheshier, *Sci. Transl. Med.*, 2017, **9**, eaaf2968.
22 Q. Tang and A. Khvorova, *Nat. Rev. Drug Discovery*, 2024, **23**, 341–364.
23 B. Hu, L. Zhong, Y. Weng, L. Peng, Y. Huang, Y. Zhao and X.-J. Liang, *Signal Transduct. Target. Ther.*, 2020, **5**, 101.
24 J. Ding, X. Zhao, S. Long, W. Sun, J. Du, J. Fan and X. Peng, *ACS Nano*, 2025, **19**, 6468–6478.

25 D. Li, Z. Cao, C. Chen, H. Li, S. He, X. Hou, M. Liang, X. Yang and J. Wang, *Biomaterials*, 2023, **302**, 122339.
26 L. Galluzzi, A. Buqué, O. Kepp, L. Zitvogel and G. Kroemer, *Nat. Rev. Immunol.*, 2017, **17**, 97–111.
27 G. Kroemer, C. Galassi, L. Zitvogel and L. Galluzzi, *Nat. Immunol.*, 2022, **23**, 487–500.
28 Z. Lyu and L. Peng, *Nat. Biomed. Eng.*, 2017, **1**, 686–688.
29 R. M. Kannan, E. Nance, S. Kannan and D. A. Tomalia, *J. Intern. Med.*, 2014, **276**, 579–617.
30 C. C. Lee, J. A. MacKay, J. M. J. Fréchet and F. C. Szoka, *Nat. Biotechnol.*, 2005, **23**, 1517–1526.
31 J. Chen, D. Zhu, X. Liu and L. Peng, *Acc. Mater. Res.*, 2022, **3**, 484–497.
32 Z. Lyu, L. Ding, A. Tintaru and L. Peng, *Acc. Chem. Res.*, 2020, **53**, 2936–2949.
33 X. Liu, D. Dhumal, P. S. Castaño, J. Liu, M. Casanova, A. C. G. Muñoz, T.-A. P. Barbacaru, A. Elkihel, W. Zhang, T. Roussel, C. Galanakou, J. Wu, E. Zerva, N. Dusetti, Y. Xia, X.-J. Liang, A. Viola, J. L. Iovanna and L. Peng, *Sci. Adv.*, 2025, **11**, eadu9948.
34 Y. Jiang, Z. Lyu, B. Ralahy, J. Liu, T. Roussel, L. Ding, J. Tang, A. Kosta, S. Giorgio, R. Tomasini, X.-J. Liang, N. Dusetti, J. Iovanna and L. Peng, *Proc. Natl. Acad. Sci. U. S. A.*, 2023, **120**, e2215308120.
35 Y. Wang, N. Gong, C. Ma, Y. Zhang, H. Tan, G. Qing, J. Zhang, Y. Wang, J. Wang, S. Chen, X. Li, Q. Ni, Y. Yuan, Y. Gan, J. Chen, F. Li, J. Zhang, C. Ou, Y. Zhao, X. Liu and X.-J. Liang, *Nat. Commun.*, 2021, **12**, 4964.
36 T. Wei, C. Chen, J. Liu, C. Liu, P. Posocco, X. Liu, Q. Cheng, S. Huo, Z. Liang, M. Fermeglia, S. Pricl, X.-J. Liang, P. Rocchi and L. Peng, *Proc. Natl. Acad. Sci. U. S. A.*, 2015, **112**, 2978–2983.
37 J. Chen, D. Zhu, B. Lian, K. Shi, P. Chen, Y. Li, W. Lin, L. Ding, Q. Long, Y. Wang, E. Laurini, W. Lan, Y. Li, A. Tintaru, C. Ju, C. Zhang, S. Pricl, J. Iovanna, X. Liu and L. Peng, *Proc. Natl. Acad. Sci. U. S. A.*, 2023, **120**, e2220787120.
38 P. Zhang, Z. Li, W. Cao, J. Tang, Y. Xia, L. Peng and J. Ma, *Adv. Mater.*, 2023, **35**, e2305215.
39 C. Ma, D. Zhu, W. Lin, Y. Li, Y. Huang, H. Zhu, M. Ye, Y. Wang, L. Peng and X. Liu, *Chem. Commun.*, 2022, **58**, 4168–4171.
40 J. Chen, A. Ellert-Miklaszewska, S. Garofalo, A. K. Dey, J. Tang, Y. Jiang, F. Clément, P. N. Marche, X. Liu, B. Kaminska, A. Santoni, C. Limatola, J. J. Rossi, J. Zhou and L. Peng, *Nat. Protoc.*, 2021, **16**, 327–351.
41 Y. Dong, Y. Chen, D. Zhu, K. Shi, C. Ma, W. Zhang, P. Rocchi, L. Jiang and X. Liu, *J. Controlled Release*, 2020, **322**, 416–425.
42 Y. Dong, T. Yu, L. Ding, E. Laurini, Y. Huang, Y. Weng, S. Lin, P. Chen, D. Marson, Y. Jiang, S. Giorgio, S. Pricl, X. Liu, P. Rocchi and L. Peng, *J. Am. Chem. Soc.*, 2018, **140**, 16264–16274.
43 Z. Lyu, B. Ralahy, T.-A. Perles-Barbacaru, L. Ding, Y. Jiang, B. Lian, T. Roussel, X. Liu, C. Galanakou, E. Laurini, A. Tintaru, S. Giorgio, S. Pricl, X. Liu, M. Bernard, J. Iovanna, A. Viola and L. Peng, *Proc. Natl. Acad. Sci. U. S. A.*, 2024, **121**, e2322403121.
44 L. Ding, Z. Lyu, T.-A. Perles-Barbacaru, A. Y.-T. Huang, B. Lian, Y. Jiang, T. Roussel, C. Galanakou, S. Giorgio, C.-L. Kao, X. Liu, J. Iovanna, M. Bernard, A. Viola and L. Peng, *Adv. Mater.*, 2024, **36**, e2308262.
45 P. Garrigue, J. Tang, L. Ding, A. Bouhlel, A. Tintaru, E. Laurini, Y. Huang, Z. Lyu, M. Zhang, S. Fernandez, L. Balasse, W. Lan, E. Mas, D. Marson, Y. Weng, X. Liu, S. Giorgio, J. Iovanna, S. Pricl, B. Guillet and L. Peng, *Proc. Natl. Acad. Sci. U. S. A.*, 2018, **115**, 11454–11459.
46 X. Liu, Y. Wang, C. Chen, A. Tintaru, Y. Cao, J. Liu, F. Ziarelli, J. Tang, H. Guo, R. Rosas, S. Giorgio, L. Charles, P. Rocchi and L. Peng, *Adv. Funct. Mater.*, 2016, **26**, 8594–8603.
47 Z. Shi, M. Artemenko, W. Yu, M. Zhang, C. Yi, P. Chen, S. Lin, Z. Bian, B. Lian, F. Meng, J. Chen, T. Roussel, Y. Li, K. K. L. Chan, P. P. C. Ip, H.-C. Lai, S. K. Y. To, X. Liu, L. Peng and A. S. T. Wong, *ACS Appl. Mater. Interfaces*, 2025, **17**, 2884–2898.
48 D. V. Krysko, A. D. Garg, A. Kaczmarek, O. Krysko, P. Agostinis and P. Vandenabeele, *Nat. Rev. Cancer*, 2012, **12**, 860–875.
49 T. Gong, L. Liu, W. Jiang and R. Zhou, *Nat. Rev. Immunol.*, 2020, **20**, 95–112.
50 P. Meier, A. J. Legrand, D. Adam and J. Silke, *Nat. Rev. Cancer*, 2024, **24**, 299–315.
51 J. L. L. B. Pang, Z. W. Zhang and C. Q. Zhang, *Eur. Cells Mater.*, 2025, **50**, 87–108.
52 J. Galon and D. Bruni, *Nat. Rev. Drug Discovery*, 2019, **18**, 197–218.
53 D. S. Chen and I. Mellman, *Nature*, 2017, **541**, 321–330.
54 A. Tasdogan, R. J. Sullivan, A. Katalinic, C. Lebbe, D. Whitaker, S. Puig, L. V. v. d. Poll-Franse, D. Massi and D. Schadendorf, *Nat. Rev. Dis. Primers.*, 2025, **11**, 23.
55 J. E. Cun, Z. He, X. Fan, Q. Pan, K. Luo, B. He and Y. Pu, *Small*, 2025, **21**, 2409875.

